Title: Analyzing volcanic-like earthquakes with distributed acoustic sensing using a short segment of the Tongan seafloor telecommunications cable

Authors:

Shunsuke Nakao[1] (s-nakao@eri.u-tokyo.ac.jp)

Mie Ichihara[1]

Masaru Nakano[2]

Taaniela Kula[3]

Rennie Vaiomounga[4]

Masanao Shinohara[1]

Affiliations:

1. Earthquake Research Institute, University of Tokyo

2. Japan Agency for Marine-Earth Science and Technology

3. Ministry of Lands and Natural Resources, Government of Tonga

4. Tonga Geological Services, Government of Tonga

Statement: This paper is a non-peer reviewed preprint submitted to EarthArXiv.

This manuscript will be submitted to Geophysical Journal International for peer review.

submitted to *Geophys. J. Int.*

Analyzing volcanic-like earthquakes with distributed acoustic sensing using a short segment of the Tongan seafloor telecommunications cable

Shunsuke Nakao[1], Mie Ichihara[1], Masaru Nakano[2], Taaniela Kula[3], Rennie Vaiomounga[4] and Masanao Shinohara[1]

[1] *Earthquake Research Institute, University of Tokyo, Yayoi* 1*, Bunkyo-ku, Tokyo* 113-0032*, Japan.*

E-mail: s-nakao@eri.u-tokyo.ac.jp

[2] *Japan Agency for Marine-Earth Science and Technology*

[3] *Ministry of Lands and Natural Resources, Government of Tonga*

[3] *Tonga Geological Services, Government of Tonga*

SUMMARY

The 2022 Hunga Tonga-Hunga Ha'apai (HTHH) eruption highlighted the need for monitoring submarine volcanoes. Distributed Acoustic Sensing (DAS), utilizing existing seafloor cables offers a promising solution. We analyze a one-week DAS dataset recorded in February 2023, one year after the eruption, using a 30-km segment of the domestic telecommunication cable in Tonga. The previous study (Nakano et al. 2024) analyzed the data for relatively large local earthquake events with clear P- and S-phases. This study focuses on unclear and small events, plenty of which are included in the data. Our objective is to create a comprehensive event catalogue and distinguish HTHH-related activity from tectonic earthquakes at the Tonga Trench. We introduce a new method to identify temporally sustained events and distinguish them from brief incoherent noise. We define a new parameter to represent the duration of sustained signal energy, with which we automatically pick events. This method successfully detects a total of 770 events, many of which are missed by conventional methods that detect the sudden increases in amplitude. The result also reveals a stable seismicity rate of approximately 110 events per day. To determine their origin, we estimate the apparent slowness of each event using a robust method combining 2D Normalized Cross-Correlation and linear fitting. We find more events with positive slowness values, which correspond to arrivals from the HTHH volcano direction, than those from the Tonga Trench (negative slowness). The result suggests that a significant fraction of the detected small earthquakes originate from the HTHH volcanic system, indicating that the volcano or its surrounding magmatic system maintains a high level of seismic activity one year after the major 2022 eruption.

Key words: Distributed acoustic sensing, Volcano monitoring, Ocean-floor seismic observations

1 INTRODUCTION

The January 2022 eruption of the Hunga Tonga-Hunga Haʻapai (HTHH) volcano in the Tongan archipelago highlighted the importance of monitoring submarine volcanic activity. Although seismic observation is essential for the monitoring of volcanic activity, no seismic stations were operational in Tonga at the time of the eruption(Garza-Girón et al. 2023; Kintner et al. 2023). The seismic network in Tonga is being revived, but the installation and maintenance of stations on remote islands are costly challenges. Furthermore, there are a few accessible islands near the HTHH.

Distributed Acoustic Sensing (DAS) observation, utilizing submarine telecommunications cables, may offer a more practical and economical solution to this problem. DAS technology, which uses a single fiber-optic cable as a dense array of seismic sensors, has recently emerged as a transformative tool for seismology, offering high spatial density. Researchers have successfully apply DAS to monitor diverse volcanic activity and environments. For instance, studies have demonstrated its capability in detecting and characterizing signals at active land volcanoes such as Mount Etna (Jousset et al. 2022; Currenti et al. 2021), Stromboli (Biagioli et al. 2024), and Azuma (Nishimura et al. 2021, 2025), as well as in challenging volcano-glacial settings, including beneath glaciers in Iceland (Klaasen et al. 2021).

These applications have enabled the detailed analysis of volcano-tectonic earthquakes, volcanic tremor, and explosive events (Nishimura et al. 2021). DAS is also used to resolve seismic structures

(Fukushima et al. 2022; Miyazawa 2024). Recently, DAS has also been applied to monitor underwater volcanic degassing (Caudron et al. 2024), demonstrating its strong potential for monitoring of targets in severe environments, including remote submarine volcanoes like HTHH. For example, observations by Nakano et al. (2024) and Nakano et al. (2026) aimed to capture volcanic earthquakes occurring from submarine volcanoes.

Nakano et al. (2024) conducted a one-week preliminary DAS observation using the existing submarine domestic telecommunications cable in Tonga. Their study showed that while DAS data had high noise levels in shallow coral reef areas, the noise significantly decreased in deeper water, indicating its suitability for deep-sea seismic observations. Nakano et al. (2024) determined the hypocenters of 17 earthquakes by picking P- and S-wave arrival times from this one-week DAS dataset and onshore seismometer data. Although many of them were tectonic events related to the Tonga Trench, one event was located beneath the HTHH crater, suggesting that volcanic activity at HTHH may had continued since the 2022 eruption. However, their analysis was limited to relatively large and clear events. To understand the activity at HTHH one year after the eruption, it is necessary to comprehensively capture the smaller earthquakes within the data.

This study aims to create a detailed seismic event catalogue from the same one-week DAS dataset used by Nakano et al. (2024) by applying a more sensitive detection method to comprehensively capture faint signals. Furthermore, we attempt to estimate the arrival directions of the detected signals using the DAS array's characteristics in order to distinguish whether they originate from the HTHH volcano or the Tonga Trench.

2 DATA

This study analyzes the Distributed Acoustic Sensing (DAS) data obtained by (Nakano et al. 2024), who performed the DAS observation on a roughly 30-km-long segment of a submarine telecommunications cable in the Kingdom of Tonga (Fig. 1). The segment was available for sensing because it had been unused after the damage caused by the eruption of the Hunga Tonga-Hunga Ha'apai (HTHH) volcano in January 2022. The observation was performed for one week in February 2023, approximately one year after the eruption.

The DAS data consist of optical phases continuously recorded at a sampling frequency of 312.5 Hz with a channel spacing of 2 m, from which we obtain a high-resolution view of the strain field along the cable using a gauge length of 30 m (Nakano et al. 2024).

Our analysis focuses specifically on the 3-km portion at the seaward end of the 30-km-long segment (Fig. 1b). The first 20 km of the cable from the land-based interrogator sits on a shallow coral reef (Fig. 1c), which is heavily influenced by ocean surface waves and local ship traffic. Beyond this

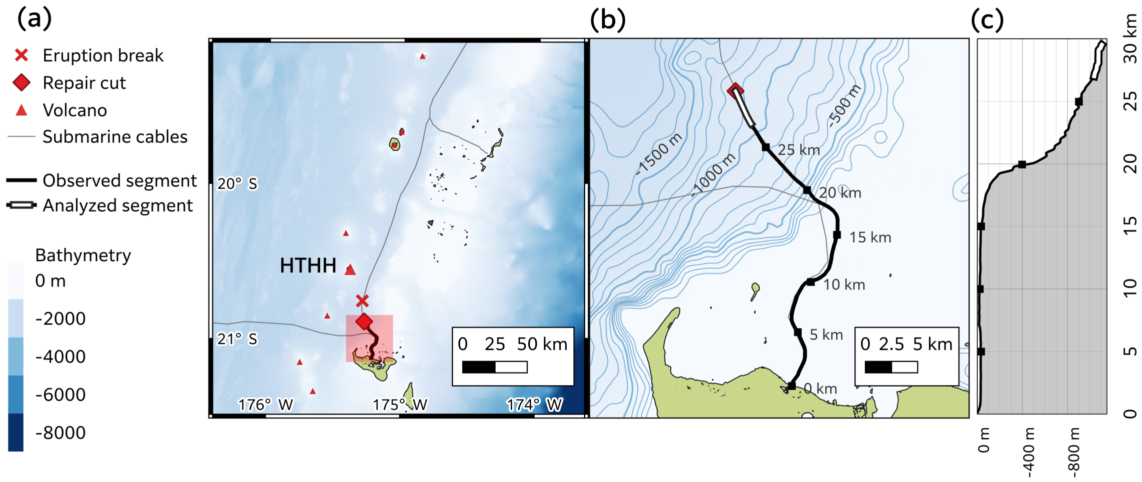

Figure 1. Map of the study area and the DAS cable configuration.

(a) Regional map showing the location of the Hunga Tonga-Hunga Haʻapai (HTHH) volcano (triangle) and the submarine cable system (thin lines). The approximately 30-km-long 'Observed segment' is highlighted as a thick line. The 'Eruption break' (a cross) indicates where the cable was severed by the January 2022 HTHH eruption, and the 'Repair cut' (a diamond) indicates the subsequent artificial cut made to facilitate repair operations.

(b) Zoomed-in map of the cable path. The hollow black rectangle highlights the 3-km 'Analyzed segment' at the seaward end of the cable. This section is approximately straight.

(c) Bathymetry profile along the cable. The horizontal distance axis corresponds to the distance markers shown along the cable path in panel (b). The profile illustrates that the cable is situated in very shallow water for the first approximately 20 km before the seafloor deepens rapidly.

The bathymetry data are from the GEBCO2024 grid (GEBCO Compilation Group 2024), and the volcano location is from the Global Volcanism Program (Global Volcanism Program 2025).

shallow region, the seafloor deepens sharply (Fig. 1c), where some sections appear to be poorly coupled with the seabed, resulting in high noise levels (Nakano et al. 2024). The last 3-km portion on a deep gentle slope exhibits the highest data quality and signal-to-noise ratio, making it the most suitable for the detailed analysis of small seismic events described in the following sections.

Hereafter, we define the array of strain time series as $d(t, ch)$, where t is time and ch is the channel index. This dataset consists of 1460 ($= N_{ch}$) channels at 2-m intervals, covering the range of 27–30 km from the landing station. The channel index increases from the landward side to the seaward side.

To evaluate our analysis methodology, we utilize a set of known events determined by Nakano et al. (2024).

3 METHODS

Volcanic earthquakes, particularly long-period (LP) events associated with fluid transport, are characterized by dominant low-frequency components in the 0.5–5 Hz range (Chouet 2003; Iguchi & Nishimura 2011; Konstantinou 2024). However, DAS data tend to exhibit high noise levels in this specific frequency band (Nakano et al. 2024). Therefore, as a compromise to balance capturing the target signals against the high noise floor, a Butterworth band-pass filter between 2 and 4 Hz is selected and applied to $d(t, ch)$ prior to the analysis.

3.1 Event Detection

We aim to detect weak volcanic signals that are likely to be missed by conventional detection algorithms, which are often tuned for distinct, high-amplitude earthquakes. To this end, we implement and evaluate several automated detection algorithms.

3.1.1 Classic STA/LTA Methods

Short-Term Average / Long-Term Average (STA/LTA) methods are widely used in seismological studies, including our previous study (Nakano et al. 2024). They have also been applied to detect volcanic events from DAS data (Klaasen et al. 2021; Biagioli et al. 2024). We test two standard STA/LTA methods: the single-channel STA/LTA method (Allen 1978) and the Network Coincidence Trigger method (Withers et al. 1998). The latter declares an event only when the STA/LTA trigger condition is met on more than a minimum number of channels across the array nearly simultaneously. The condition reduces the false detections caused by noise in individual channels.

3.1.2 Lower-Envelope Method

We design a new method targeting events with emergent or slow onsets. First, we compress the squared array data, $d(t, ch)^2$, (Fig. 2a), to a single time series, $P_{\text{med}}(t)$, that is the median power across all the N_{ch} channels:

$$P_{\text{med}}(t) = \underset{ch=1\ldots N_{ch}}{\text{median}} \left[d(t, ch)^2 \right] . \tag{1}$$

We take the median values to effectively suppress spatially incoherent noise and call $P_{\text{med}}(t)$ 'median power'. It has a physical unit of squared strain and is thus dimensionless. Second, we track the baseline fluctuations of the background noise by computing a lower 'envelope' of $P_{\text{med}}(t)$. Here, the 'envelope' is not such a formal envelope as derived from a Hilbert transform but consists of the minimum value of $P_{\text{med}}(t)$ in a 101-sample window sliding with time. Events are then identified by applying a simple thresholding trigger to the lower-envelope waveform.

3.1.3 Duration-based Method

We design another method to identify temporally sustained events and distinguish them from brief incoherent noise. We define a new parameter for calculating the STA/LTA ratio to detect events based on the duration of sustained signal energy, rather than a sudden increase in amplitude.

First, we calculate the median power, $P_{\text{med}}(t)$, as above using eq. (1). Next, which is the core of the method, we transform $P_{\text{med}}(t)$ into a "duration" waveform, $Dur(t)$, in the following two steps, as illustrated in Fig. 2b and c.

(i) **Defining a Threshold:** A dynamic threshold, $P_{\text{thresh}}(t)$, is established by computing a moving average of $P_{\text{med}}(t)$:

$$P_{\text{thresh}}(t) = \frac{1}{T_{\text{avg}}} \int_{t-T_{\text{avg}}/2}^{t+T_{\text{avg}}/2} P_{\text{med}}(\tau) d\tau, \tag{2}$$

where T_{avg} is the window length (60 s). $P_{\text{thresh}}(t)$ provides the threshold that adapts to long-period variations in the background noise level (Fig. 2b).

(ii) **Calculating Duration:** The algorithm then calculates a duration waveform, $Dur(t)$:

$$Dur(t) = \begin{cases} \min\{\tau > 0 \mid P_{\text{med}}(t+\tau) < P_{\text{thresh}}(t+\tau)\}, \\ \qquad\qquad\qquad\qquad \text{if } P_{\text{med}}(t) > P_{\text{thresh}}(t), \\ 0, \qquad\qquad\qquad\qquad \text{otherwise.} \end{cases} \tag{3}$$

It represents the duration from any given time, t, when $P_{\text{med}}(t) > P_{\text{thresh}}(t)$ to the time when $P_{\text{med}}(t)$ next drops below $P_{\text{thresh}}(t)$ (Fig. 2c).

Then, we apply a 0.1 Hz low-pass filter to $Dur(t)$ to smooth out minor fluctuations and consolidate event durations into a final characteristic function, $C(t)$. Specifically, we use the impulse response, $h(t)$, of the fourth order Butterworth low-pass filter:

$$C(t) = Dur(t) * h(t) = \int_{-\infty}^{\infty} Dur(\tau) h(t-\tau) d\tau. \tag{4}$$

Finally, we apply the standard STA/LTA algorithm to $C(t)$, to detect events (Fig. 2d). The STA/LTA ratio, $R(t)$, is given by:

$$R(t) = \frac{\frac{1}{T_{\text{STA}}} \int_{t-T_{\text{STA}}}^{t} C(\tau) d\tau}{\frac{1}{T_{\text{LTA}}} \int_{t-T_{\text{LTA}}}^{t} C(\tau) d\tau}, \tag{5}$$

where $T_{STA} = 20$ s and $T_{LTA} = 240$ s. We pick an event time when $R(t)$ rises above a threshold, which we set 2.5. We represent the n-th event time by t^n. We do not distinguish events occurring within one minute.

After the event detections, we cut $d(t, ch)$ from 30 s before to 45 s after the event time, t^n, for

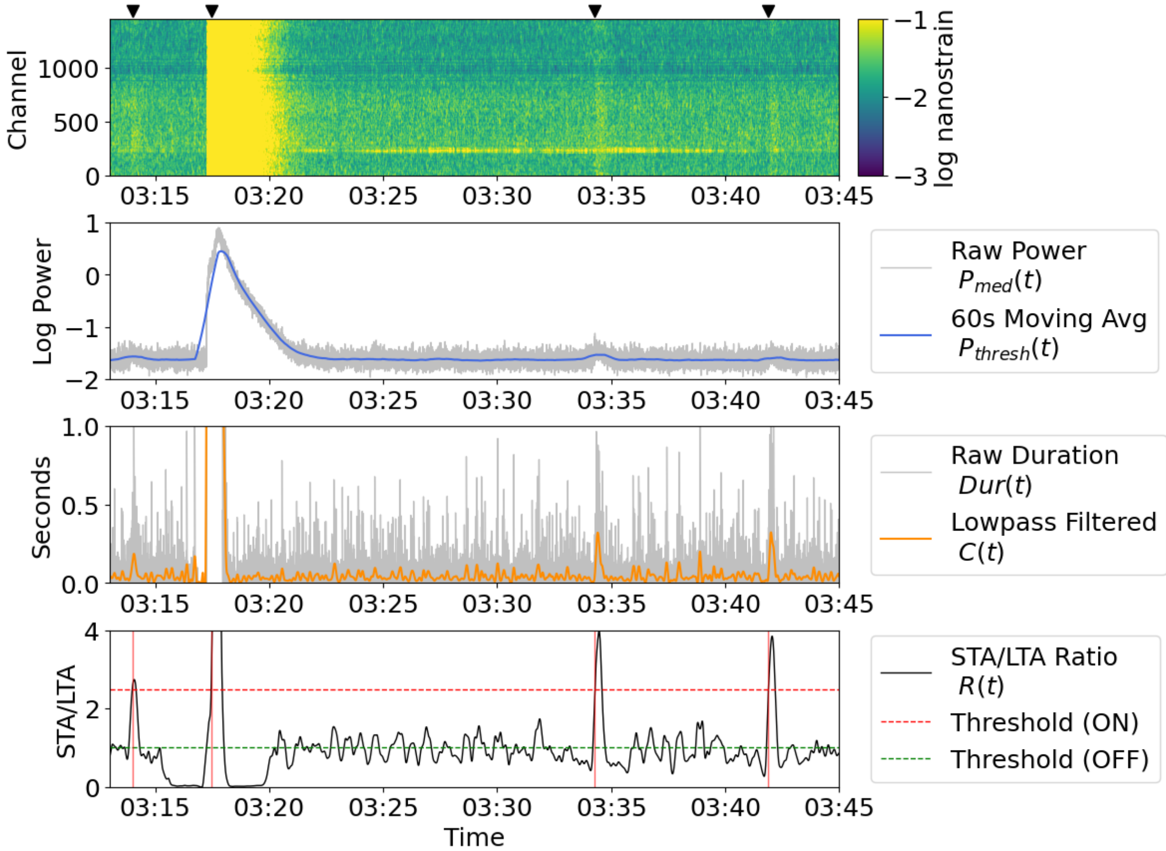

Figure 2. Procedural steps of the duration-based event detection algorithm. **(a)** The input 2D seismic power data as a function of channel and time. The black triangles indicate the final detection times determined in panel (d). **(b)** The median power across all channels (grey line, $P_{med}(t)$), creating a single time series that is robust against spatially incoherent noise. A 60-s moving average is then computed (blue line, $P_{thresh}(t)$) to define a dynamic threshold that adapts to long-period variations in the background noise.

(c) The "duration", a new parameter (grey line, $Dur(t)$), calculated as the time for which the median power continuously exceeds the dynamic threshold from (b). The duration time series is then low-pass filtered (orange line, $C(t)$) to smooth out short-term fluctuations.

(d) The characteristic function from applying a classic STA/LTA algorithm (black line, $R(t)$) to the filtered duration signal from (c). An event is triggered when the function exceeds the predefined threshold (dashed line).

each event, which we call an event array, $d^n(t, ch)$. When we limit the frequency range, a band-pass filter is applied to the longer data before cutting the event array to avoid the edge effects.

3.2 Apparent Slowness Estimation

We estimate the apparent slowness of each event array, $d^n(t, ch)$, extracted by the Duration-based Method. We develop a new method for estimating inter-channel time delays for the stable estimation

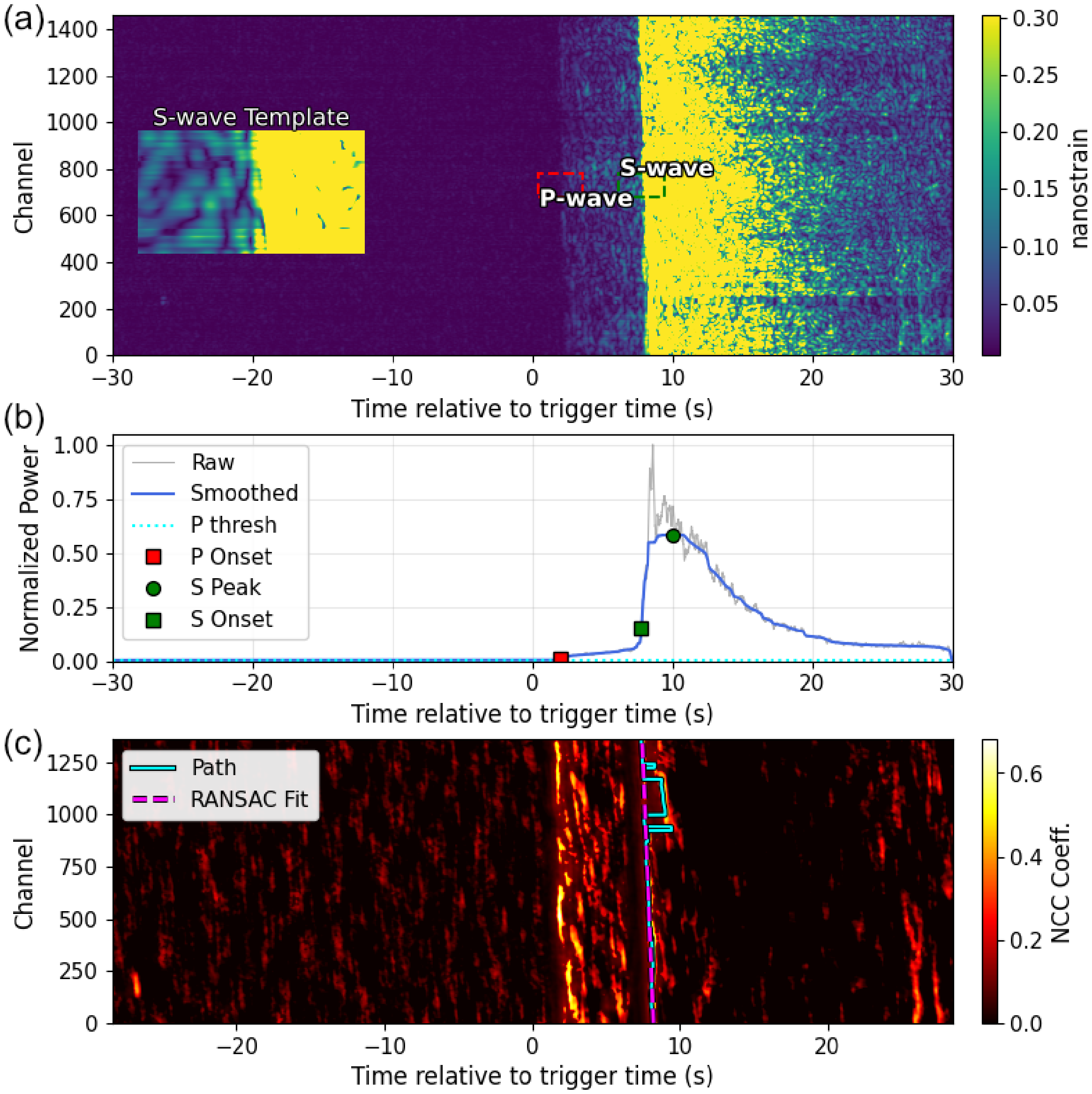

Figure 3. Workflow of the apparent slowness estimation method using 2D Normalized Cross-Correlation (NCC) and RANSAC, illustrated with a representative seismic event.

(a) Processed Data & Template Location. The 2D envelope of the preprocessed data (1–10 Hz bandpass) for the 3-km array segment. Dashed rectangles indicate the locations identified for the P-wave (red) and S-wave (green) templates.

(b) 1D Power Profile & Phase Detection. The median power across all channels (blue line), used to detect phase arrivals. The P-wave (red) is identified by an SNR threshold, while the S-wave (green) is identified by its prominent peak. The circle marks the peak, and squares mark the onsets, which are used as the temporal centers for the templates. S-wave onset (green square) is equivalent to t_o^n.

(c) NCC Map & Slowness Fit. The resulting NCC similarity map was computed using the template from (a). The algorithm extracts the optimal travel-time path (cyan line) by finding the maximum NCC score within a search window at each channel, followed by median smoothing. A robust linear fit is then applied to the smoothed path using RANSAC (magenta line) to determine the apparent slowness (e.g., 0.290 s/km for this event).

of the slowness. It consists of three main steps: (1) automatic peak detection, (2) 2D Normalized Cross-Correlation (NCC), and (3) robust linear fitting using RANSAC (Random Sample Consensus). Here, we use the frequency range of 1–10 Hz, in which we obtain good NCC scores.

3.2.1 Automatic peak detection

The raw DAS data is contaminated by coherent noise that appears simultaneously across all channels. This noise is likely attributed to instrumental sources, such as mechanical vibrations of the interrogator or opto-electronic fluctuations, which exhibit an effectively infinite apparent velocity across the array. In contrast, the seismic signals of interest propagate along the array with finite apparent velocities, resulting in time delays between channels. Since the seismic phases are not synchronized across the array at any given instant t, their contribution to the spatial mean is minimized due to destructive interference. Therefore, we apply a common-mode noise removal process to enhance the signal-to-noise ratio. This process assumes that subtracting the spatial mean at each time step removes the simultaneous noise while preserving the propagating seismic signals. The operation is defined as follows:

$$d^{n\prime}(t, ch) = d^n(t, ch) - \underset{ch=1\ldots N_{ch}}{\text{mean}} \left[d^n(t, ch) \right]. \tag{6}$$

Then, we compute the envelope of $d^{n\prime}(t, ch)$ for each channel, using the Hilbert transform, which we denote $d^n_{env}(t, ch)$ for the n-th event.

We also calculate the median power time series, $P^n_{med}(t)$, using eq.(1) for $d^{n\prime}(t, ch)$. We identify the major energy peak of $P^n_{med}(t)$ by searching for local maxima that satisfy constraints on minimum height (above the 65th percentile), peak prominence (based on the 85th percentile), and peak separation (at least 3.0 s). The onset time t^n_o is defined as the last time index $t < t_{peak}$ satisfying:

$$P^n_{med}(t) \leq P_{base} + 0.2 \times (P^n_{med}(t_{peak}) - P_{base}), \tag{7}$$

where P_{base} is the pre-event noise level(Fig. 3b).

3.2.2 Normalized Cross-Correlation

We extract an array of 1000 time points $\times$ 100 channels of $d^n_{env}(t, ch)$ centered at $(t^n_o, N_{ch}/2)$, which we use as the template of the n-th event, d^n_{tmp} (Fig. 3a).

We then compute the Normalized Cross-Correlation (NCC) between the template and the individual 100-channel sub-arrays of the entire $d^n_{env}(t, ch)$ using OpenCV's(Bradski 2000) fast matchTemplate function. This process generates a 2D similarity map of the n-th event, $NCC^n_{map}(\tau, ch)$, where τ represents the time lag and ch denotes the channel position. The NCC value at a given location (τ, ch) is calculated as follows:

$$NCC^n_{map}(\tau, ch) = \frac{\sum_{p=1}^{1000}\sum_{q=1}^{100}\left(d^n_{tmp}(p,q) - \bar{d}^n_{tmp}\right)\left(d^n_{env}(\tau+p, ch+q) - \bar{I}\right)}{\sqrt{\sum_{p=1}^{1000}\sum_{q=1}^{100}\left(d^n_{tmp}(p,q) - \bar{d}^n_{tmp}\right)^2}\sqrt{\sum_{p=1}^{1000}\sum_{q=1}^{100}\left(d^n_{env}(\tau+p, ch+q) - \bar{I}\right)^2}} \quad (8)$$

where p and q serve as the temporal and spatial indices, respectively, within the template and sub-arrays. $\bar{d}^n_{tmp}$ denotes the mean value of the template, and $\bar{I}$ represents the mean value of the local sub-array of d^n_{env} covered by the template at position (τ, ch). This zero-mean normalization ensures robustness against amplitude scaling and DC offsets.

A waveform from an ordinary earthquake has a P-wave phase before the main oscillation with S-waves. PhaseNet algorithm has been proposed and used to automatically pick the onsets of the P- and S-phases (Zhu & Beroza 2019; Baillet et al. 2025). However, volcanic earthquakes do not necessary exhibit clear P- and S-phases. Therefore, we focus on the main oscillation part, assuming it is an S-wave. When a noticeable preceding phase exists, we use competitive template matching in the following way to avoid the contamination of the P-wave. We define the preceding phase onset, t^n_p, as the first time index where the smoothed median power time series exceeds a signal-to-noise ratio (SNR) threshold based on the pre-event noise level. The threshold is defined as $\mu_{noise} + \alpha\sigma_{noise}$, where μ_{noise} and σ_{noise} are the median and standard deviation of the initial 15 s baseline window, and α is the SNR parameter (set to 1.5). Using a template array centered at $(t^n_p, N_{ch}/2)$, we calculated another similarity map, $NCC^n_{pmap}(\tau, ch)$. We reduce the correlation scores in the 'Main' map, $NCC^n_{map}(\tau, ch)$, to its 30 % at each location (τ, ch) where $NCC^n_{map}(\tau, ch) < NCC^n_{pmap}(\tau, ch)$. This step ensures that the subsequent path-finding focuses only on energy clearly associated with the 'Main' phase (Fig. 3c).

To extract the travel-time path from the similarity map, we define a limited search window centered around the expected arrival time, assuming an apparent velocity larger than 1 km/s. We then find the time lag, $\tau_{max}(ch)$, of the maximum $NCC^n_{map}(\tau, ch)$ within this window for each ch. The extracted path, $\tau_{max}(ch)$, may contain local jumps due to noise. We apply a median filter with the window size of 21 to smooth the path.

3.2.3 Linear fitting

Finally, we perform a weighted linear regression on the smoothed path using the RANSAC algorithm (Fischler & Bolles 1981). The NCC score at each path point is used as the weight for the fit. RANSAC effectively identifies and excludes outliers if any remain after the above-mentioned median filtering. The final linear fit is performed using only the inlier data points identified by RANSAC to determine the robust slope (slowness, in s/km) and intercept.

Table 1. Comparison of detection algorithm performance over a 24-hour test period. The duration-based method demonstrates the highest F1-score, indicating the best balance between precision and recall.

Method	TP	FP	FN	Precision	Recall	F1-Score
STA/LTA	58	23	17	0.716	0.773	0.744
Lower-Envelope	55	5	20	0.917	0.733	0.815
Duration-based	**71**	**7**	**4**	**0.910**	**0.947**	**0.928**

TP: True Positives, FP: False Positives, FN: False Negatives.

3.3 Amplitude Calibration Model

To establish an empirical relationship between the observed amplitude and the magnitude of the event, we used the major energy peak of $P^n_{med}(t)$ (defined in Section 3.2.1) as the amplitude A.

To fit the data to a seismological attenuation model, we first converted the strain amplitude A to velocity amplitude A_v. This conversion was based on a plane-wave approximation, where A is multiplied by the apparent velocity (Wang et al. 2018). Although Trabattoni et al. (2023) point out that this approximation limits the correct conversion to only dominant phases and does not preserve relative amplitudes between phases with different velocities, it has been shown to be effective for magnitude estimation based on dominant phases.

We fitted the data of the known events from Nakano et al. (2024) to an empirical relationship (eq. 9) based on a generalized seismological attenuation model, which assumes negligible anelastic attenuation. The model for the velocity amplitude A_v at a hypocenter distance r from an earthquake of magnitude M is expressed as:

$$\log_{10}(A_v) = 0.85M - 1.73\log_{10}(r) + c, \tag{9}$$

based on Watanabe (1971). We performed a linear regression using our dataset (A_v, M, r) to solve for the constant offset term c.

4 RESULTS

4.1 Event Detection

Table 1 compares the performance of the three automatic methods explained in Section 3.1 (STA/LTA, lower-envelope, and duration-based) with a manually picked catalogue for a 24-hour period on February 7, 2023. We evaluate their performances by the F1-score, which measures the balance between the precision and recall. The results show that the duration-based method achieves the F1-score as high as

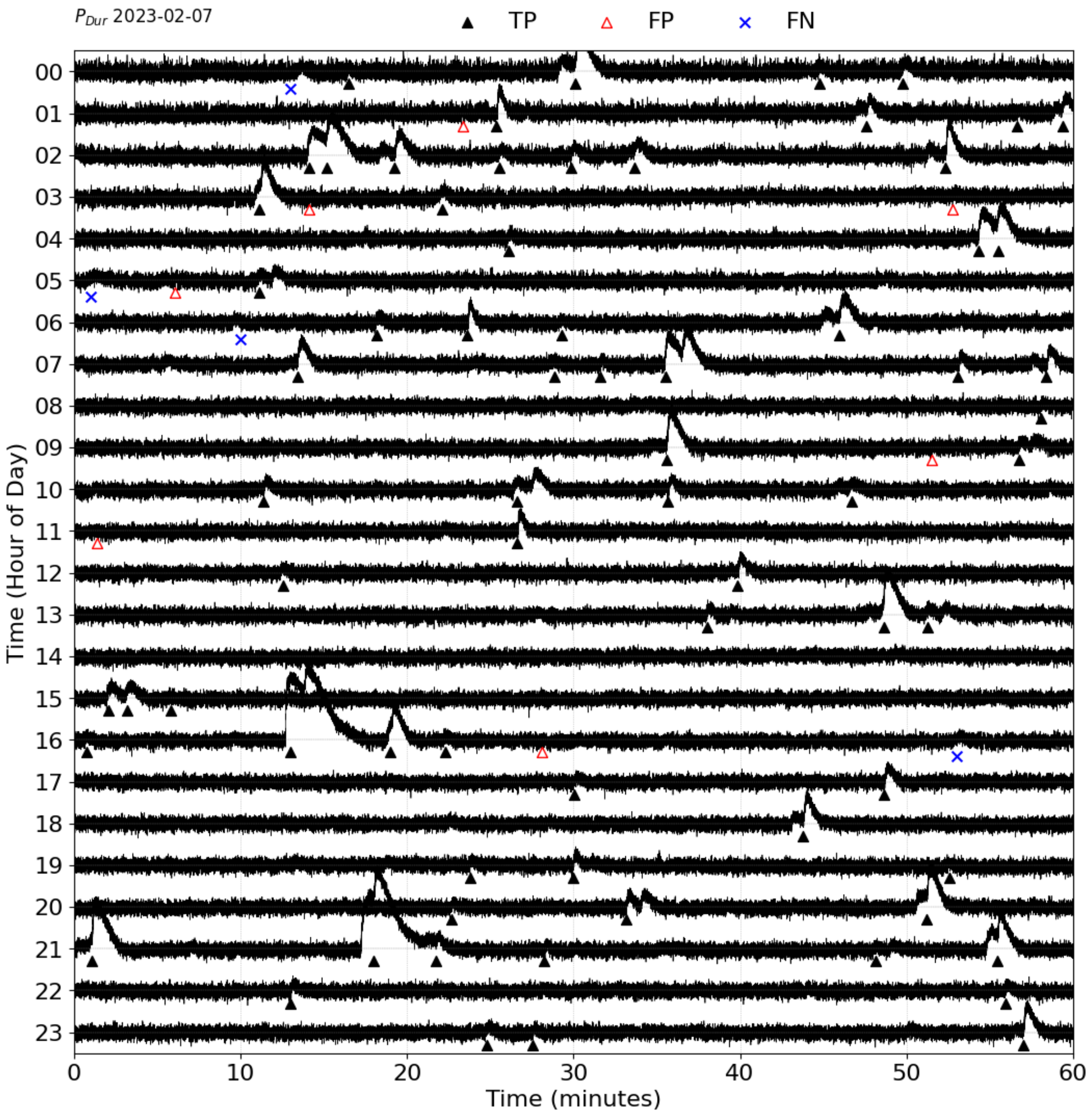

Figure 4. Twenty-four-hour drum plot of P_{Dur} (7 February 2023). Each row shows one hour. Upward triangles mark automatic triggers (black: True Positive; red: False Positive); blue x mark False Negative.

0.941, which is the highest of the three methods. Figure 4) demonstrates the excellent performance of the duration-based method. We therefore use it for the analysis of the full dataset.

Applying the duration-based algorithm to the entire one-week observation period yields a catalogue of 770 discrete events. The cumulative number of events increases almost linearly with time, indicating a persistent and stable rate of seismicity of approximately 110 events per day. No significant temporal clustering or swarm-like activity is observed during this period.

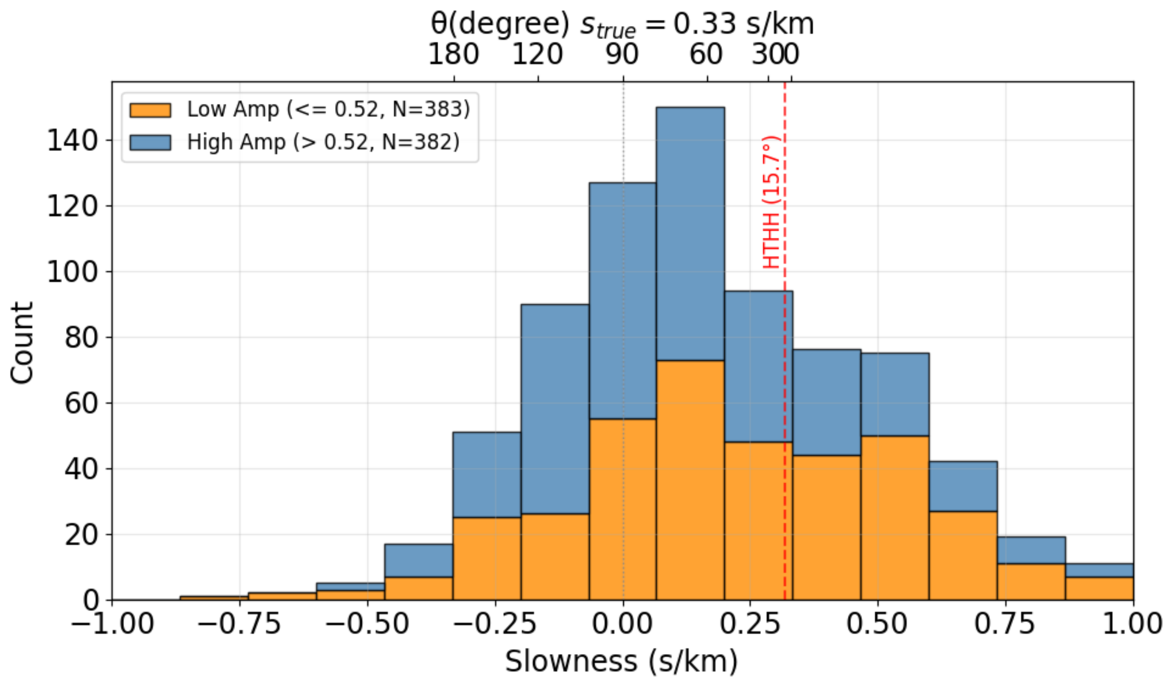

Figure 5. Histogram of apparent slowness estimated for the S-wave or unidentified phases detected in this study. A positive slowness value indicates a wave propagating from higher to lower channel numbers.

A new catalogue includes the 770 events, with the onset time (t_o^n), the major energy peak of $P_{med}^n(t)$, and other results from the subsequent analyses (Supplementary material).

4.2 Apparent Slowness Estimation

We apply our NCC and RANSAC methods to estimate the apparent slowness for the Main phase of the 770 events. Figure 5 shows the distribution of the apparent slownesses. The distribution is unimodal and broad. The modal bin (the peak of the histogram) is not centered at 0 s/km, but rather lies in the positive slowness range of 0.07 to 0.20 s/km (150 counts), and the distribution shows a clear skew towards positive slowness values.

We evaluate the accuracy of the slowness estimation by the ratio of the inlier points accepted by the RANSAC algorithm, the residual of the linear fitting, and the amplitude of each event. These parameters are included in the catalogue (Supplementary material). We have confirmed that the slowness distribution shape does not depend on these accuracy measures.

4.3 Amplitude Calibration

Figure 6(a) compares the velocity amplitude (A_v) distribution, derived from the major energy peak of $P_{med}^n(t)$ (Section 3.2.1), of the new catalogue with that of the earthquake events analyzed by Nakano

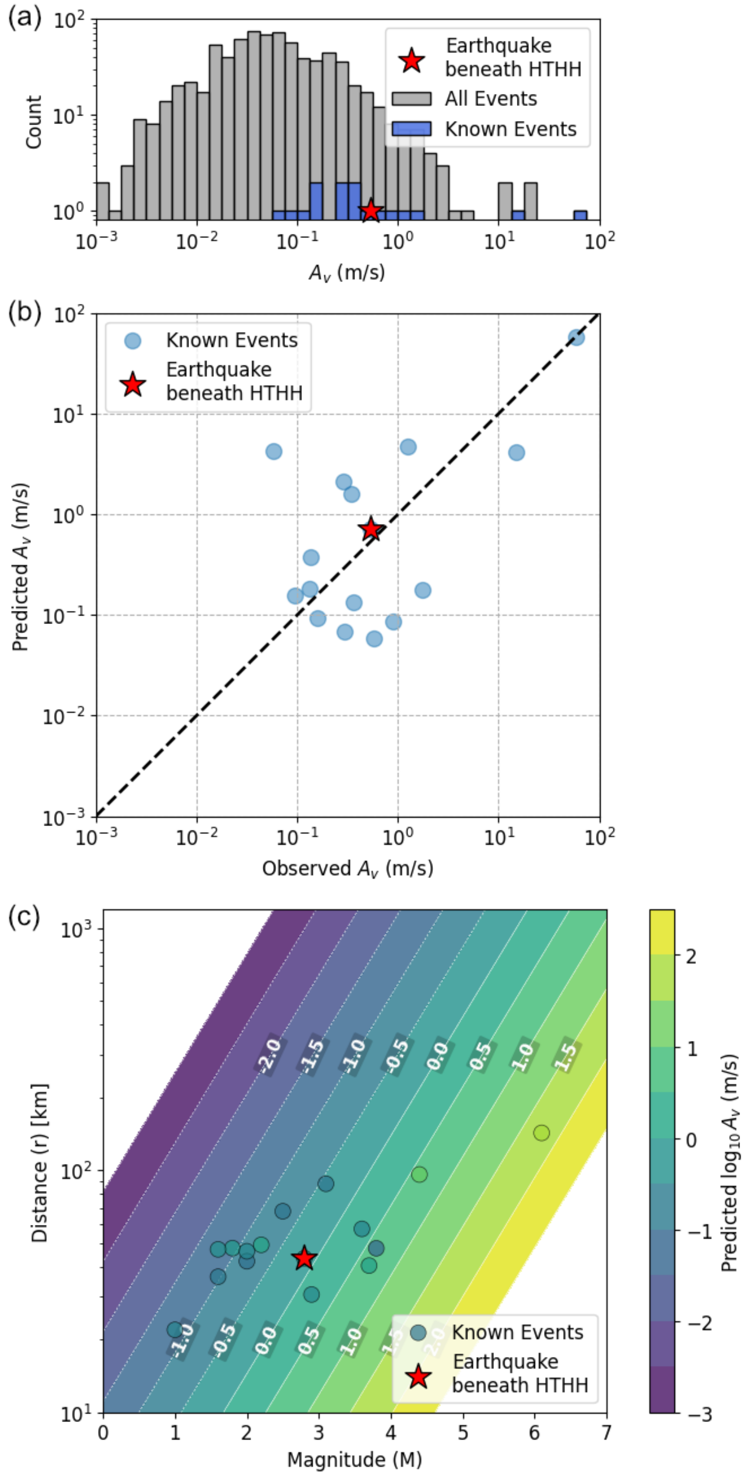

Figure 6. Amplitude analysis of known seismic events used for calibration.

(a) Histogram of $\log_{10} A_v$ for all 770 detected events (grey) and the subset of known, catalogued events (blue). The known events represent the higher-amplitude portion of the overall seismicity.

(b) Predicted versus observed RMS amplitude for the known events, based on the fitted attenuation model described in the text. The points cluster around the 1:1 reference line (dashed), indicating a good model fit.

(c) Contour map of the fitted amplitude-distance-magnitude relationship (background color). Circles show the observed data points from the known events, coloured by their observed log10(amplitude).

et al. (2024). The histogram of the new event catalogue is strongly skewed towards low amplitudes, highlighting that the majority of the 770 events are weak earthquakes.

We fit the velocity amplitudes (A_v) of the events in the previous catalogue (Nakano et al. 2024) to the attenuation model (eq. 9) described in Section 3.3. Using the A_v values derived from this study, along with the magnitude M and distances r from Nakano et al. (2024), we performed a linear regression to solve for the constant offset term c. This model provides a robust first-order fit to the data, as shown by the comparison between predicted and observed amplitudes (Fig. 6b).

We use this fitted model (eq. 9) to create the amplitude-distance-magnitude relationship shown in Fig. 6(c), which contextualizes the amplitudes of our newly detected events. The colors show the A_v amplitudes expected by the model. The observed amplitude-distance-magnitude relationship for the known events (circles colored by their A_v) are also plotted, demonstrating the consistency of the data with the model. The purpose of Fig. 6(c) is to infer the magnitudes of the events in our new catalogue. We see that the modal $\log_{10}(A_v)$ of -1.5 (Fig. 6a) corresponds to an earthquake of approximately M1.3 if they occur at a 50 km distance, or M2.0 at a 100 km distance, according to our model.

5 DISCUSSION

Our study demonstrates that the high spatial density of DAS plays a critical role in detecting small and unclear volcanic earthquakes. Conventional detection methods often struggle with low-amplitude signals due to high background noise levels on individual channels. However, by leveraging the dense spatial sampling of DAS (1460 channels over 3 km) 4, we were able to compute the spatial median power, $P_{med}(t)$5. This process effectively suppresses spatially incoherent noise6, significantly enhancing the signal-to-noise ratio compared to single-point observations.

The apparent slowness distribution of the S-wave (or unidentified phases) for the detected events (Fig. 5) shows a broad shape, having a peak near 0 s/km. The distribution is asymmetric, with more events observed having positive slowness than those with negative slowness. The apparent slowness, s_{app}, and the angle of incidence, θ, has a relationship,

$$s_{app} = s_{true} \cos\theta, \tag{10}$$

where s_{true} is the slowness determined by the S-wave velocity of the medium, and $\theta = 0$ is defined as the seaward direction along the cable. Based on eq. (10) we can interpret the slowness to the direction of signal arrival.

We assume that the events, detected in this study, consist of signals from at least two distinct sources: (1) tectonic seismicity from the Tonga Trench, which is one of the most seismically active subduction zones, and (2) activity originating from the HTHH volcano or its vicinity. Negative slow-

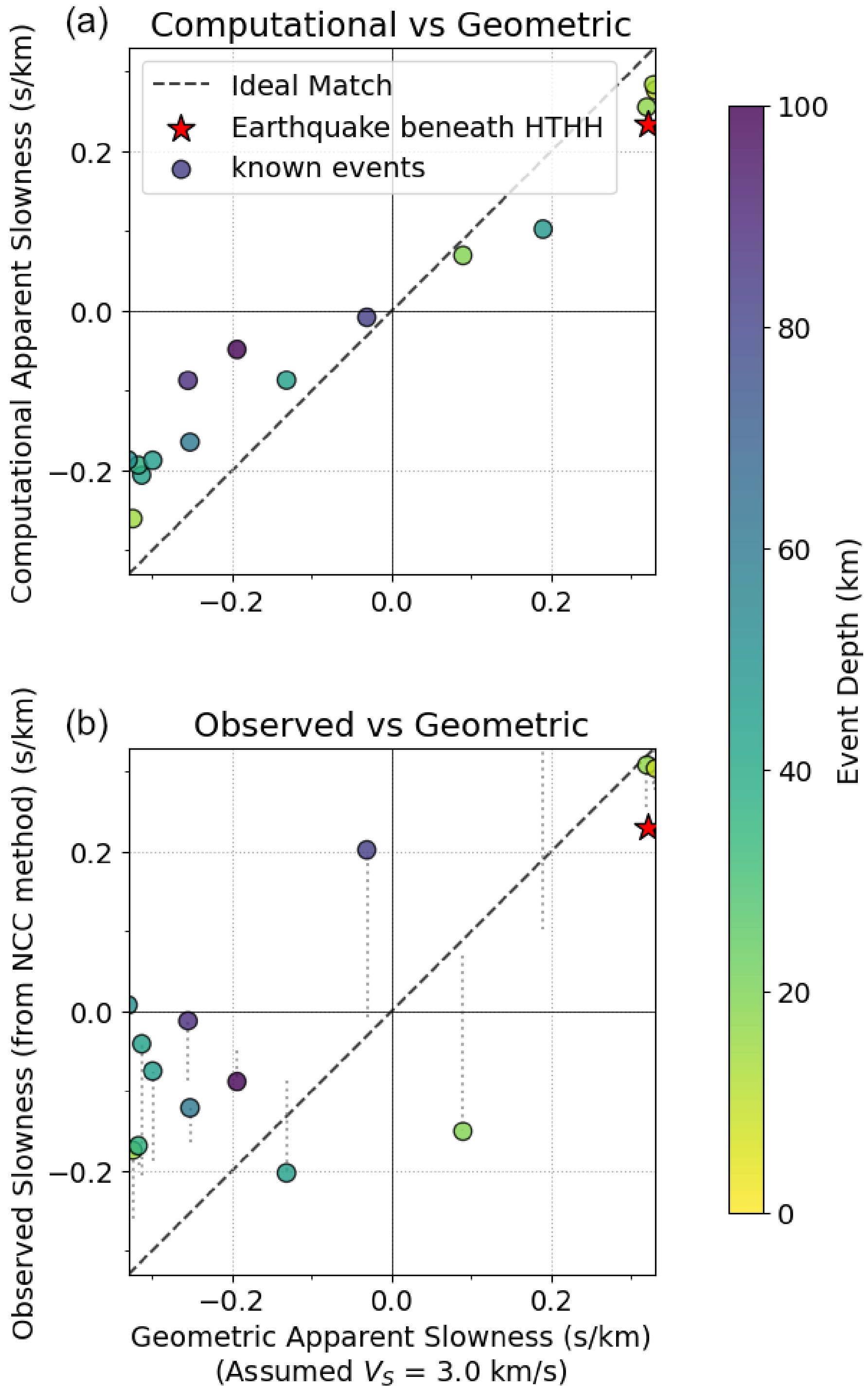

Figure 7. Comparison of apparent slowness values calculated by different methods.

Relationships between geometric apparent slowness (x-axis) and **(a)** the computational apparent slowness (y-axis), calculated using the ObsPy TauP toolkit (Crotwell et al. 1999) with a 1D velocity model from Crawford et al. (2003), and **(b)** the observed apparent slowness (y-axis), derived from the inverse of the measured array velocity. In both plots, event depth is indicated by color. Black dashed lines represent the ideal 1:1 match. Gray dotted lines in (b) connect the corresponding y-axis values from plot (a) to plot (b) for the same event, illustrating the deviation of inferred slowness from model-based slowness. Event numbers are shown as labels for each data point.

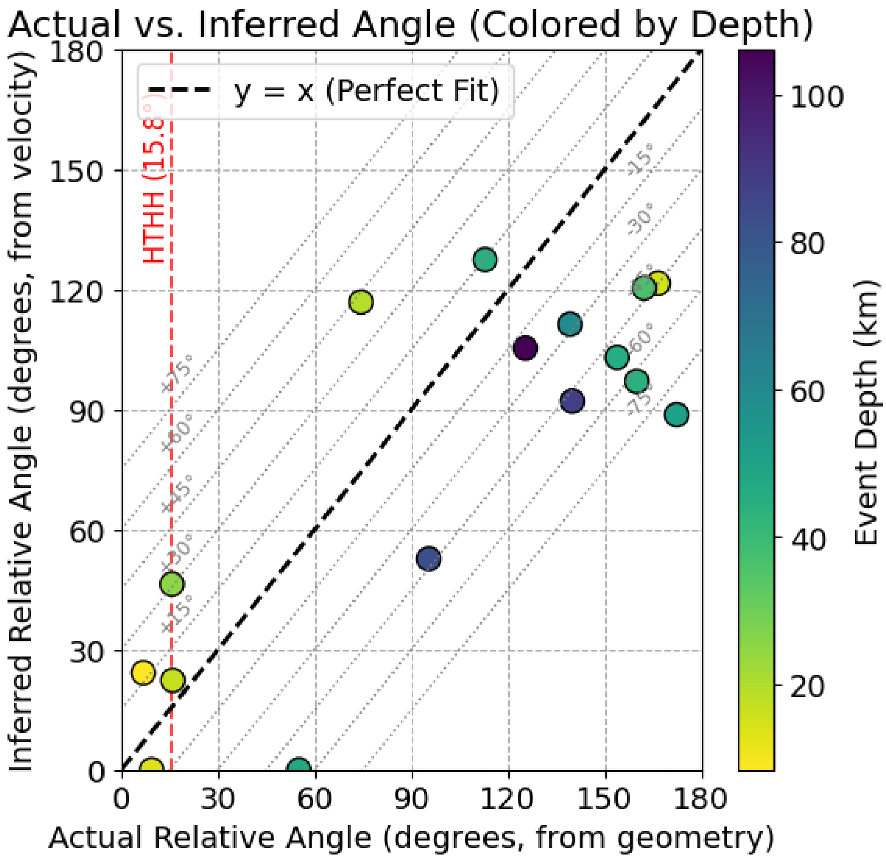

Figure 8. Validation of the estimated arrival angles. The scatter plot compares the geometric relative angle (x-axis) with the angle inferred from apparent velocity measurements (y-axis), assuming a reference velocity of $V_{true} = 3.0$ km/s. Colors indicate the focal depth of each event. The vertical red dashed line marks the relative direction of the HTHH volcano ($15.8°$). Gray dotted lines denote deviation intervals of $15°$.

ness indicates propagation from the lower to the higher channel numbers (see caption of Fig. 5). For our DAS array, which is oriented at an azimuth of approximately $325°$, measured clockwise from the North, negative slowness corresponds to the azimuths of arrival from $55°$ to $135°$. The events with negative slowness likely originate from the Tonga Trench earthquakes. On the other hand, events with positive slowness propagate from the opposite directions, where active volcanoes in Tonga exist, including HTHH at $\sim 340°$. Waves from HTHH arrive nearly parallel to the array (end-fire, $\theta \approx 15°$), meaning their apparent slowness s_{app} should be close to the true slowness s_{true} that is the possible maximum absolute value (observed as a positive value in this case).

We examine the interpretation of the slowness to the source direction more quantitatively, using the known regional earthquake source locations from the catalogue by Nakano et al. (2024). We calculated a ”computational apparent slowness” from each source using the TauP toolkit (Crotwell et al. 1999) based on the P-wave velocity structure of Crawford et al. (2003) with an assumed constant $V_p/V_s =$

1.73. The P-wave model linearly connects 1.8 km/s, 3.0 km/s, and 6.0 km/s at the depths of 0, 0.8, and 4.9 km, respectively. Alternatively, we use the geometric incident angle from each source as θ in eq. (10) with an assumed S-wave velocity of 3.0 km/s ($s_{true} = 0.33$ s/km) to estimate s_{app}, which we call ”geometric apparent slowness.” Figure 7(a) compares the ”computational apparent slowness” and ”geometric apparent slowness”. They show good agreement, especially for relatively shallow earthquakes. The result confirms that the simple geometric model is a reasonable approximation for interpreting slowness values in relation to source directions in this study.

Next, Figure 7(b) compares the above ”geometric apparent slowness” with the ”observed slowness” obtained by the NCC-based method (section 3.2.2) to evaluate the accuracy of the method. The errors are significant for the two points with geometric apparent slowness close to zero. Their observed values have large absolute values with opposite signs. The other events with larger absolute values of apparent slowness exhibit better agreement between the observed and geometric values. The earthquake whose hypocenter was located directly beneath HTHH (Nakano et al. 2024) has a large positive apparent slowness (the geometric value of 0.32 s/km and the observed value of 0.23 s/km). Therefore, it is important to have a good resolution for large apparent slowness.

We convert the slowness values on both axes in Fig. 7(b) to the angles using eq. (10) and present them in Fig. 8 to compare the ”Inferred Relative Angle” (derived from the observed slowness) with the ”Actual Relative Angle” (derived from the geometry). This comparison revealed the significant angle discrepancies for some events. The discrepancies do not depend on the event depth or distance.

The errors in the geometric angles or slowness values from the actual incident angles are likely inherited from the uncertainties in the S-wave velocity structure and the cable orientation. On the other hand, a plausible error source of the ”observed” angles or slowness values is a potential contamination from P-wave coda. Even if we tried targeting only the S-wave phases, the contamination could have degraded the quality of the S-wave template used for the NCC analysis, especially in events with short P-S times.

The majority of the 770 events we newly detected were unclear events for which P- and S-phases could not be clearly separated, in contrast to the clear seismic events used for the validation. This unclear characteristic may reflect the nature of volcanic seismicity (e.g., long-period events or tremor), which is often characterized by low-frequency content and less distinct onsets.

The slowness estimates for these unclear events inevitably include some error. Nevertheless, we consider the sign (positive or negative) and the order of magnitude (near zero or large) of the estimated slowness to be sufficiently robust for broadly classifying the wave’s arrival direction (e.g., ”Trench-side” vs. ”HTHH-side”).

The slowness distribution (Fig. 5) shows that our data contains signals from multiple source regions. Many events may be associated with the background seismicity of the Tonga Trench. However, we infer that the events with large positive slowness have their origin near the HTHH volcano. The result of the amplitude calibration (Fig. 6) indicates that their magnitudes are as large as $M1$. If all of these events are from the HTHH, the volcano was generating tens of M1-class events per day. One of the most significant findings of this study is that the HTHH (or its surrounding magmatic system) may have maintained a high level of seismic activity even one year after the 2022 eruption.

DATA AVAILABILITY

The event catalogue and median power data of 3-km-long analyzed section($P_{\mathrm{med}}(t)$), and the code to reproduce Figs. 2 and 4–8 are available in the GitHub repository at `https://github.com/dasvlc/Supplementary`. The location data of the cable is subject to confidentiality agreements with Tonga Cable Ltd. and cannot be publicly shared.

ACKNOWLEDGMENTS

We are grateful to the Tonga Cable Ltd. for permissions to use the domestic fiber optic cables and much support during our DAS experiment. We thank Dr. Daisuke Suetsugu and Prof. Takao Ohminato for their assistance in the observation. This study was supported by Science and Technology Research Partnership for Sustainable Development (SATREPS) funded by Japan International Cooperation Agency (JICA)/Japan Science and Technology Agency (JST) (Grant 23727132). SN carried out the research supported by International Graduate Program for Excellence in Earth-Space Science (IGPEES), a World-leading Innovative Graduate Study (WINGS) Program, the University of Tokyo. This study is also funded by ERI of the University of Tokyo, JAMSTEC, and Tonga Geological Services (TGS).

AUTHOR CONTRIBUTINONS

SN developed the methodology, analyzed the data, drafted the manuscript, and prepared all figures. MI conceptualized the research, secured funding, and contributed to manuscript drafting. MS and MN supervised the analyses and manuscript preparation. MI, MN, TK, RV, and MS contributed to data acquisition for this study.

CONFLICT OF INTEREST

The authors declare that they have no known competing financial interests or personal relationships that could have appeared to influence the work reported in this paper.

REFERENCES

Allen, R. V., 1978. Automatic earthquake recognition and timing from single traces, *Bulletin of the seismological society of America*, **68**(5), 1521–1532.

Baillet, M., Rivet, D., Trabattoni, A., Cheze, J., Peix, F., Ambrois, D., van den Ende, M., Vernet, C., Strumia, C., Potin, B., et al., 2025. Automatic earthquake catalogs from a permanent das offshore network, *Journal of Geophysical Research: Solid Earth*, **130**(10), e2025JB031565.

Biagioli, F., Métaxian, J.-P., Stutzmann, E., Ripepe, M., Bernard, P., Trabattoni, A., Longo, R., & Bouin, M.-P., 2024. Array analysis of seismo-volcanic activity with distributed acoustic sensing, *Geophysical Journal International*, **236**(1), 607–620.

Bradski, G., 2000. The OpenCV Library, *Dr. Dobb's Journal of Software Tools*.

Caudron, C., Miao, Y., Spica, Z. J., Wollin, C., Haberland, C., Jousset, P., Yates, A., Vandemeulebrouck, J., Schmidt, B., Krawczyk, C., et al., 2024. Monitoring underwater volcano degassing using fiber-optic sensing, *Scientific reports*, **14**(1), 3128.

Chouet, B., 2003. Volcano seismology, *Pure and Applied Geophysics*, **160**(3), 739–788, doi: 10.1007/pl00012556.

Crawford, W. C., Hildebrand, J. A., Dorman, L. M., Webb, S. C., & Wiens, D. A., 2003. Tonga ridge and lau basin crustal structure from seismic refraction data, *Journal of Geophysical Research: Solid Earth*, **108**(B4), doi: https://doi.org/10.1029/2001JB001435.

Crotwell, H., Owens, T., & Ritsema, J., 1999. The taup toolkit: Flexible seismic travel-time and raypath utilities, *Seismological Research Letters*, **70**, doi: 10.1785/gssrl.70.2.154.

Currenti, G., Jousset, P., Napoli, R., Krawczyk, C., & Weber, M., 2021. On the comparison of strain measurements from fibre optics with dense seismometer array at etna volcano (italy), *Solid Earth Discussions*, **2021**, 1–19.

Fischler, M. A. & Bolles, R. C., 1981. Random sample consensus: a paradigm for model fitting with applications to image analysis and automated cartography, *Commun. ACM*, **24**(6), 381–395, doi: 10.1145/358669.358692.

Fukushima, S., Shinohara, M., Nishida, K., Takeo, A., Yamada, T., & Yomogida, K., 2022. Detailed s-wave velocity structure of sediment and crust off sanriku, japan by a new analysis method for distributed acoustic sensing data using a seafloor cable and seismic interferometry, *Earth, Planets and Space*, **74**(1), 92.

Garza-Girón, R., Lay, T., Pollitz, F., Kanamori, H., & Rivera, L., 2023. Solid earth–atmosphere interaction forces during the 15 january 2022 tonga eruption, *Science Advances*, **9**(2), eadd4931.

GEBCO Compilation Group, 2024. The GEBCO 2024 Grid, doi: 10.5285/19641efa-3298-3571-e063-6c86abc0b310.

Global Volcanism Program, 2025. Volcanoes of the World, v. 5.2.8 (6 May 2025), `https://volcano.si.edu`, doi: 10.5479/si.GVP.VOTW4-2013.

Iguchi, M. & Nishimura, T., 2011. *Volcanic Earthquakes and Tremor in Japan*, Kyoto University Press.

Jousset, P., Currenti, G., Schwarz, B., Chalari, A., Tilmann, F., Reinsch, T., Zuccarello, L., Privitera, E., & Krawczyk, C. M., 2022. Fibre optic distributed acoustic sensing of volcanic events, *Nature communications*, **13**(1), 1753.

Kintner, J. A., Yeck, W. L., Earle, P. S., Prejean, S., & Pesicek, J. D., 2023. High-precision characterization of seismicity from the 2022 hunga tonga-hunga ha'apai volcanic eruption, *Seismological Society of America*, **94**(2A), 589–602.

Klaasen, S., Paitz, P., Lindner, N., Dettmer, J., & Fichtner, A., 2021. Distributed acoustic sensing in volcano-glacial environments—mount meager, british columbia, *Journal of Geophysical Research: Solid Earth*, **126**(11), e2021JB022358.

Konstantinou, K., 2024. A review of the source characteristics and physical mechanisms of very long period (vlp) seismic signals at active volcanoes, *Surveys in Geophysics*, **45**(1), 117–149.

Miyazawa, M., 2024. Inclined bending seismic reflection layer in the crust illuminated by distributed fibre-optic-sensing measurements in western japan, *Scientific Reports*, **14**(1), 25877.

Nakano, M., Ichihara, M., Suetsugu, D., Ohminato, T., Ono, S., Vaiomounga, R., Kula, T., & Shinohara, M., 2024. Monitoring volcanic activity with distributed acoustic sensing using the tongan seafloor telecommunications cable, *Earth, Planets and Space*, **76**(1), 25.

Nakano, M., Nakajima, T., Araki, E., Sugioka, H., Ito, A., Matsumoto, H., Yokobiki, T., Tonegawa, T.,& Ono, S., 2026. Seismic activities at Kikai Caldera, Japan, detected using distributed acoustic sensing via seafloor telecommunication cables, *Journal of Volcanology and Geothermal Research*, **469**, 108498.

Nishimura, T., Emoto, K., Nakahara, H., Miura, S., Yamamoto, M., Sugimura, S., Ishikawa, A., & Kimura, T., 2021. Source location of volcanic earthquakes and subsurface characterization using fiber-optic cable and distributed acoustic sensing system, *Scientific reports*, **11**(1), 6319.

Nishimura, T., Morisaku, F., Emoto, K., Nakahara, H., Yamamoto, M., & Miura, S., 2025. Complex principal component analysis of volcanic earthquakes at azuma volcano, japan, recorded by a distributed acoustic sensing system (das) for the hypocenter determination, *Journal of Volcanology and Geothermal Research*, **463**, 108343.

Trabattoni, A., Biagioli, F., Strumia, C., van den Ende, M., Scotto di Uccio, F., Festa, G., Rivet, D., Sladen, A., Ampuero, J. P., Métaxian, J.-P., & Stutzmann, É., 2023. From strain to displacement: using deformation to enhance distributed acoustic sensing applications, *Geophysical Journal International*, **235**(3), 2372–2384, doi: 10.1093/gji/ggad365.

Wang, H. F., Zeng, X., Miller, D. E., Fratta, D., Feigl, K. L., Thurber, C. H., & Mellors, R. J., 2018. Ground motion response to an ml 4.3 earthquake using co-located distributed acoustic sensing and seismometer arrays, *Geophysical Journal International*, **213**(3), 2020–2036.

Watanabe, H., 1971. Determination of earthquake magnitude at regional distance in and near japan, *Zisin 2*, **24**, 189–200.

Withers, M., Aster, R., Young, C., Beiriger, J., Harris, M., Moore, S., & Trujillo, J., 1998. A comparison of select trigger algorithms for automated global seismic phase and event detection, *Bulletin of the Seismological Society of America*, **88**(1), 95–106.

Zhu, W. & Beroza, G. C., 2019. Phasenet: a deep-neural-network-based seismic arrival-time picking method, *Geophysical Journal International*, **216**(1), 261–273.

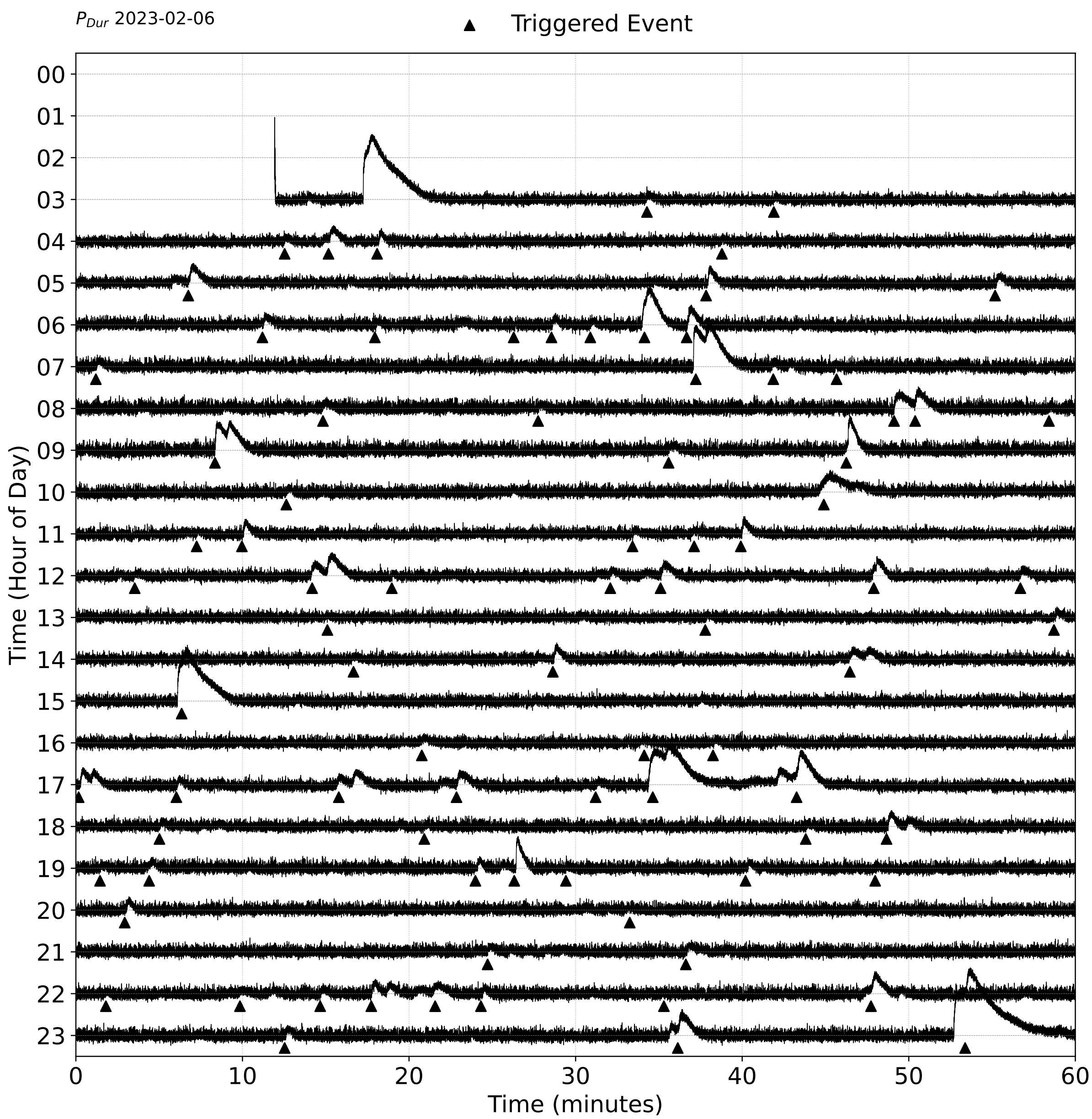

Figure S1: Twenty-four-hour drum plot of P_{Dur} on 6 February 2023. Each row shows one hour. Upward triangles mark automatic triggers.

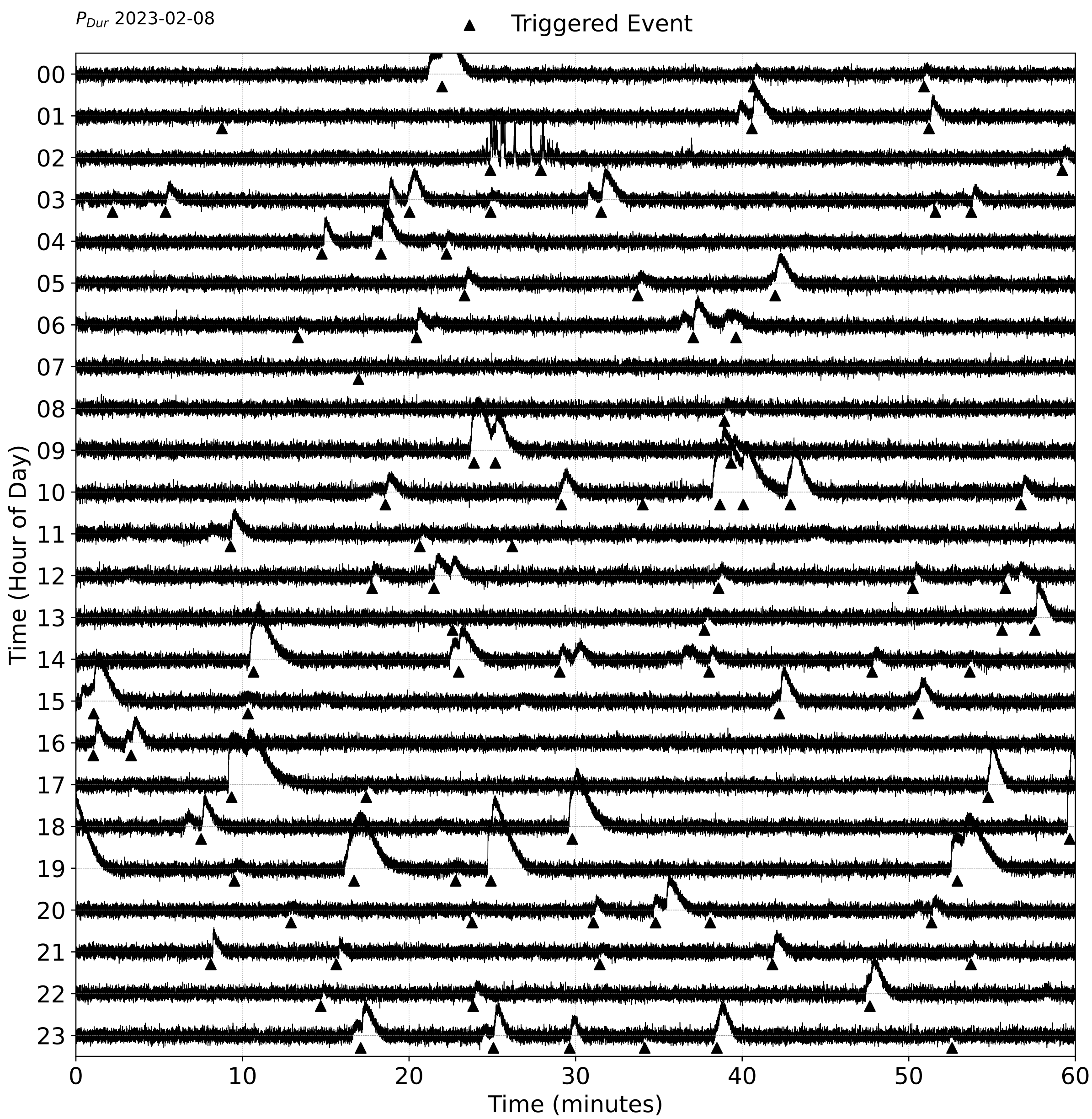

Figure S2: Twenty-four-hour drum plot of P_{Dur} on 8 February 2023. Each row shows one hour. Upward triangles mark automatic triggers.

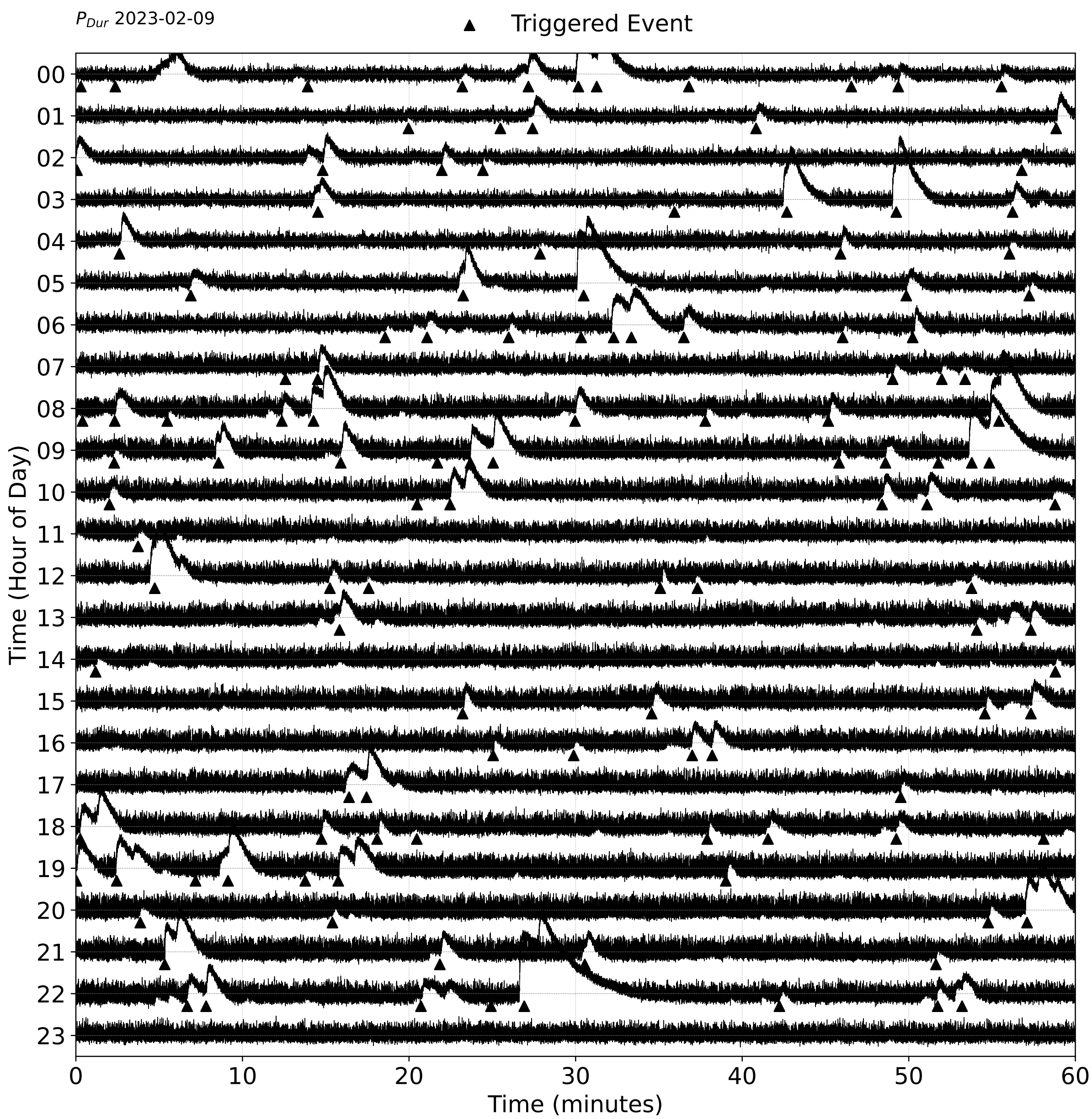

Figure S3: Twenty-four-hour drum plot of P_{Dur} on 9 February 2023. Each row shows one hour. Upward triangles mark automatic triggers.

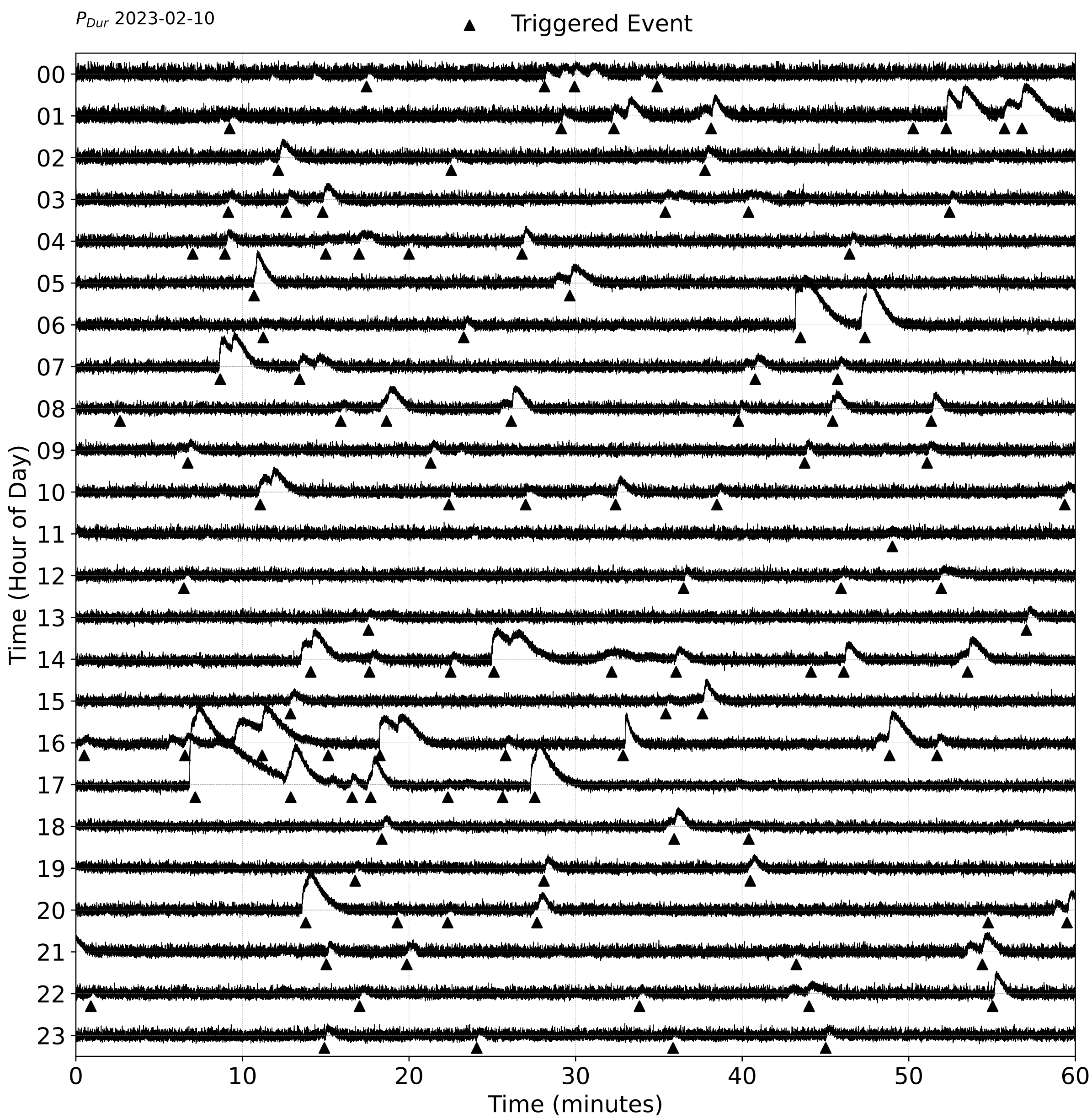

Figure S4: Twenty-four-hour drum plot of P_{Dur} on 10 February 2023. Each row shows one hour. Upward triangles mark automatic triggers.

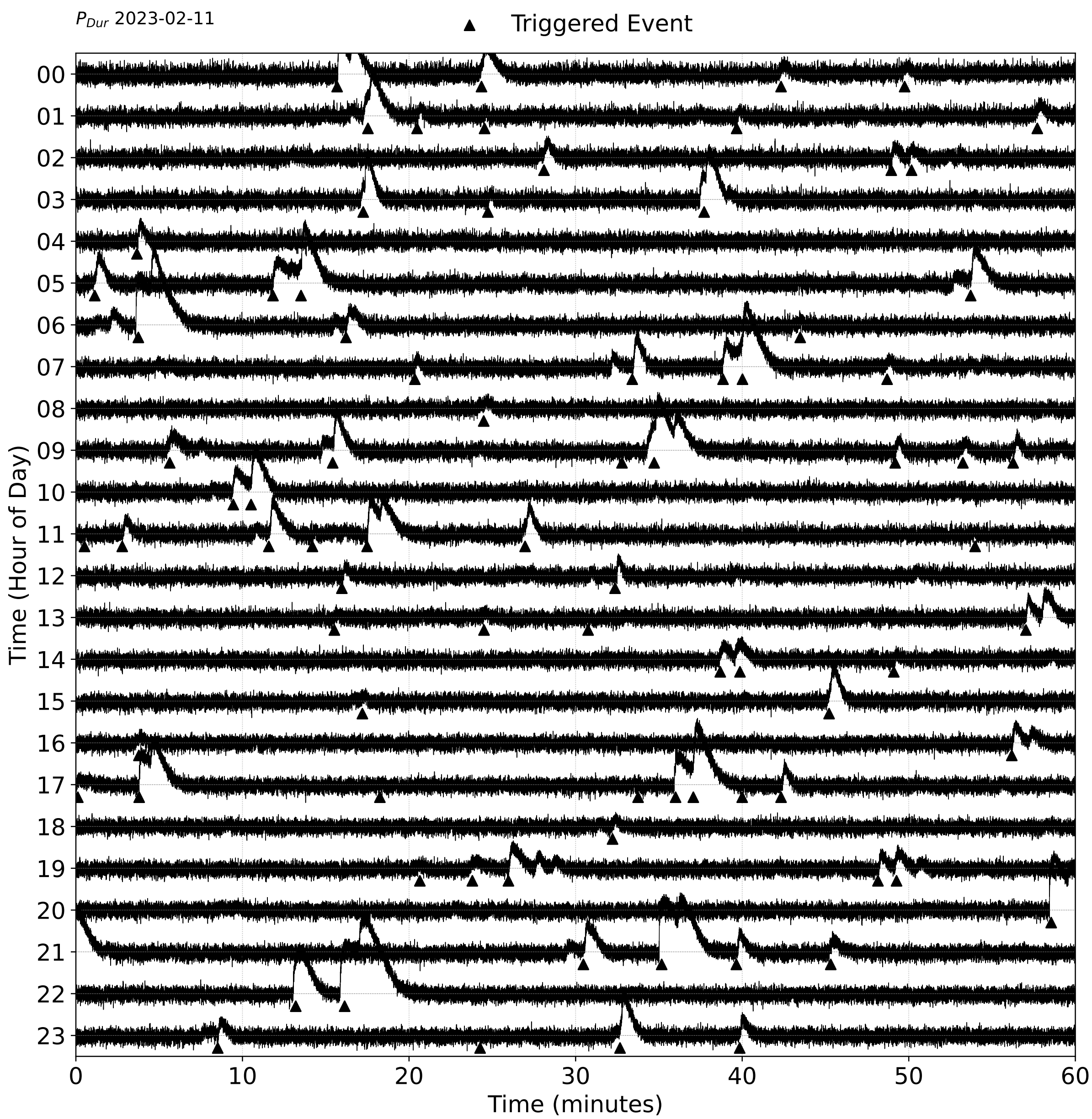

Figure S5: Twenty-four-hour drum plot of P_{Dur} on 11 February 2023. Each row shows one hour. Upward triangles mark automatic triggers.

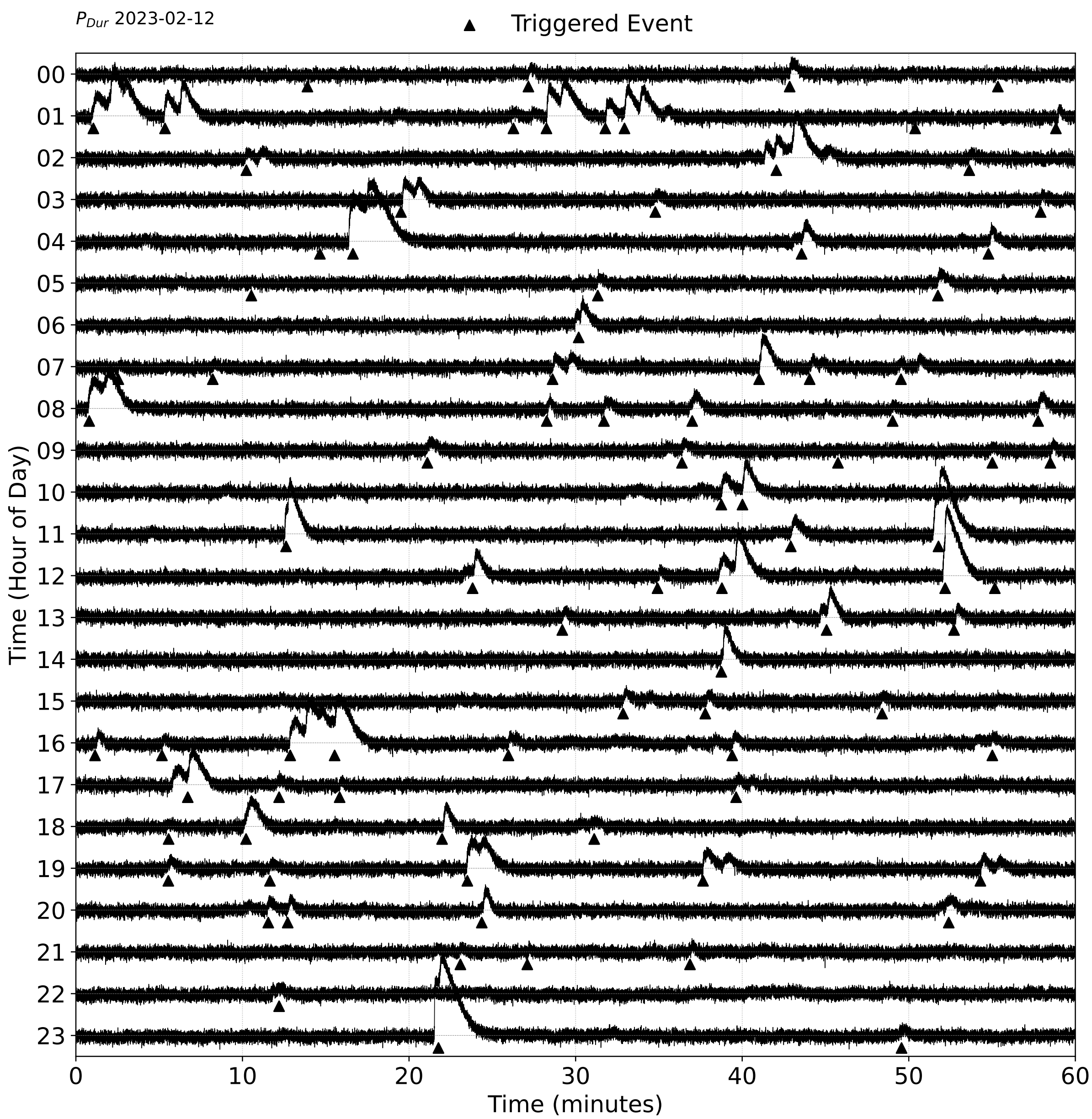

Figure S6: Twenty-four-hour drum plot of P_{Dur} on 12 February 2023. Each row shows one hour. Upward triangles mark automatic triggers.

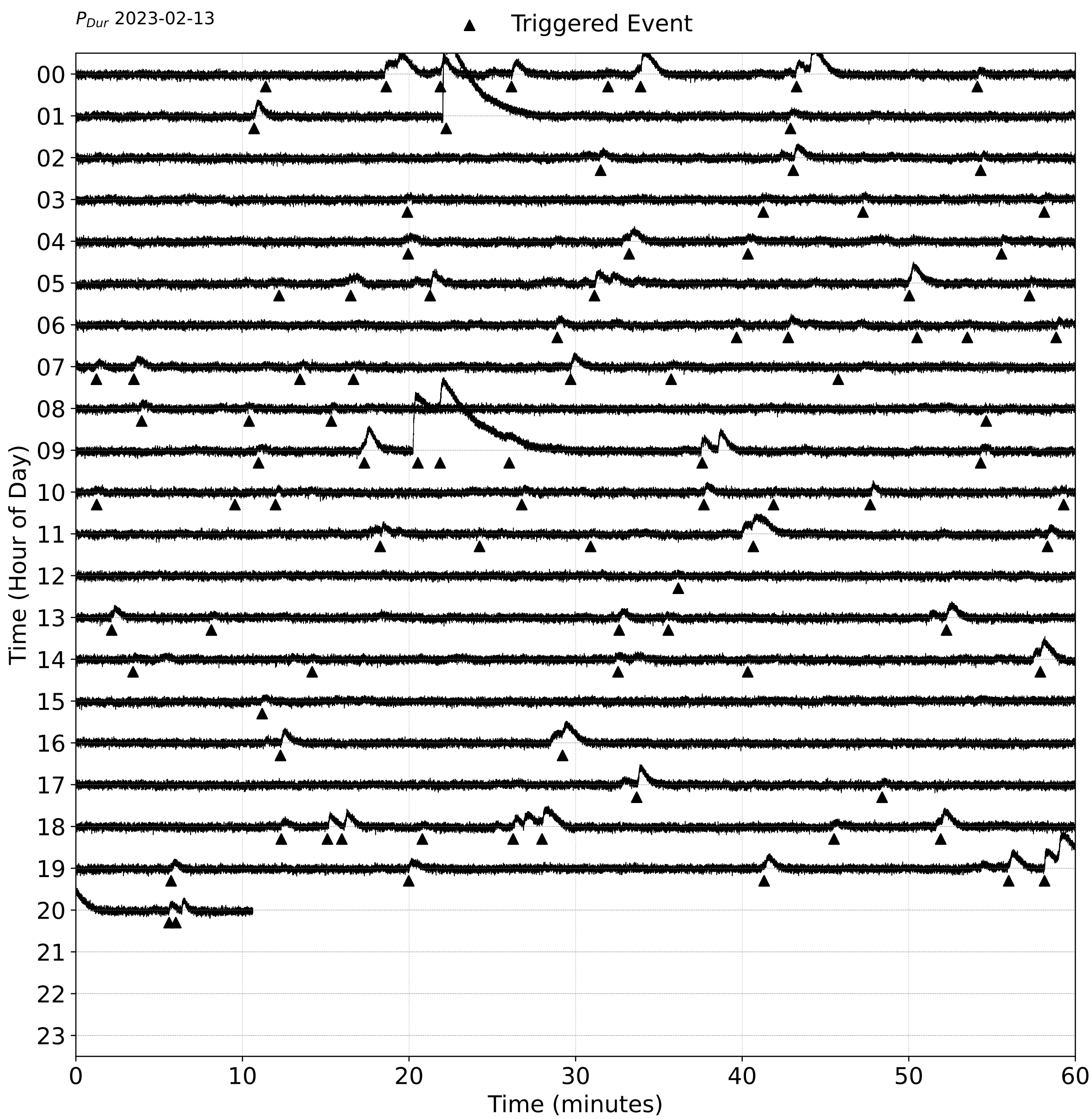

Figure S7: Twenty-four-hour drum plot of P_{Dur} on 13 February 2023. Each row shows one hour. Upward triangles mark automatic triggers.

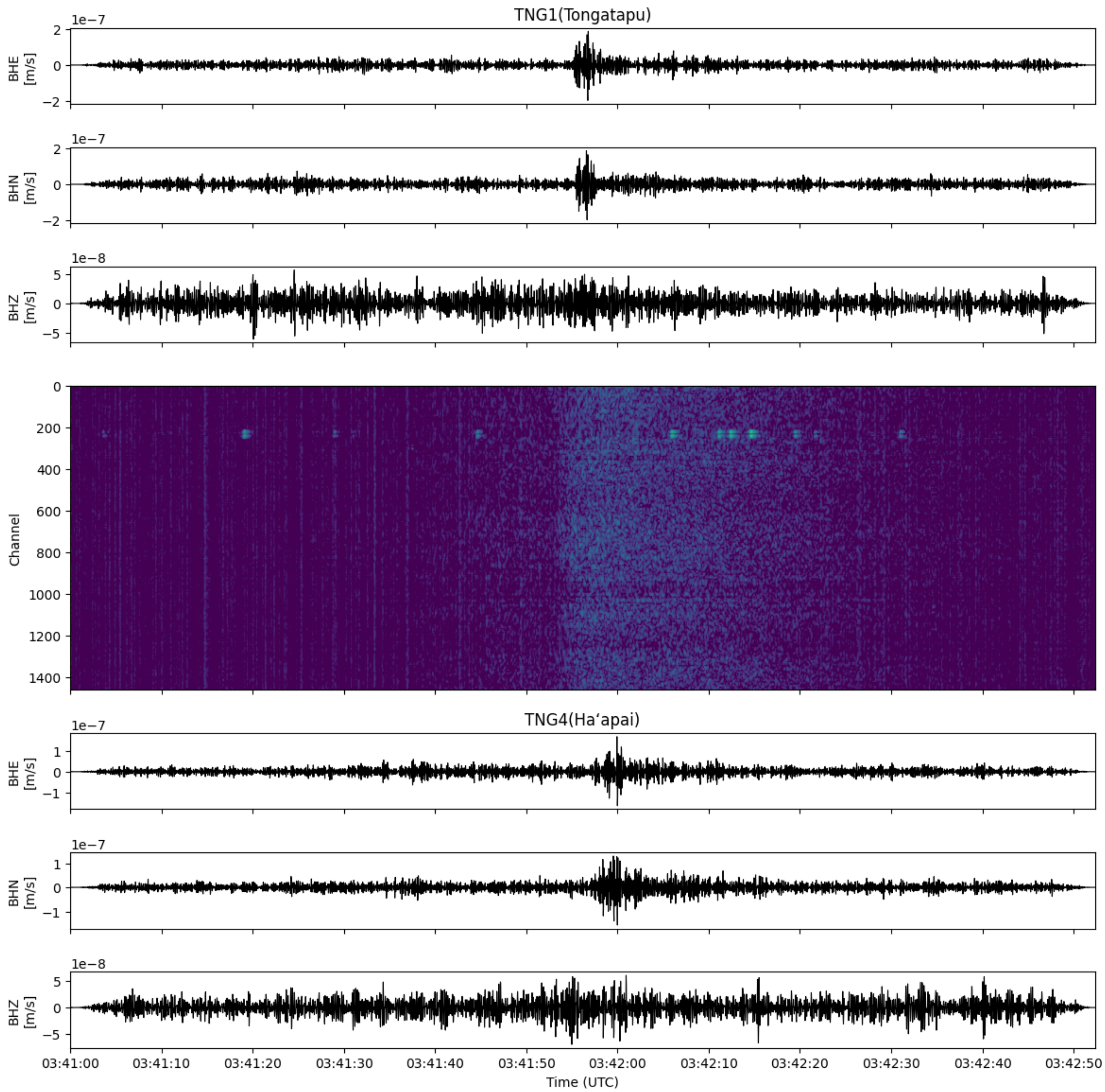

Figure S8: Comparison of DAS and land seismometer records. TNG1 is located approximately 40 km SSE of DAS, while TNG4 is located about 150 km NE of DAS.